ADVANCED MATERIALS INTERFACES
www.advmatinterfaces.de

Highly Stable Doped Barium Niobate Based Electrocatalysts for Effective Electrochemical Coupling of Methane to Ethylene

Luke H. Denoyer, Angelica Benavidez, Fernando H. Garzon, and Kannan P. Ramaiyan**

Methane conversion into value-added products such as olefins and aromatics is gaining increased attention in the wake of new natural gas reserve discoveries. Electrochemical oxidative coupling of methane (E-OCM) provides better product selectivity as the product distribution can be controlled by applied potential as well as the oxide ion flux. Here a new catalyst based on Mg and Fe codoped barium niobate perovskites is reported. The prepared perovskites show excellent chemical stability in CH_4-rich environments up to 925 °C while showing methane activation properties from 600 °C. E-OCM measurements indicate an ethylene production rate of 277 µmol cm^{-2} h^{-1} with a faradaic efficiency of 20% at 1 V and durable operation for six continuous days. X-ray photoelectron spectroscopic measurements indicate significant Nb valency reorganization that can be the reason for its chemical stability. Nevertheless, the surface area of the catalyst is significantly lower and requires improvements in synthesis methodologies to improve catalytic activity further. The exceptional chemical stability of this perovskite material under methane exposure at high temperatures has significant importance as this material can be used as a catalyst and/or support in a wide variety of applications relevant for efficient energy conversion and storage.

1. Introduction

Efficient on-site conversion of methane to value-added chemicals such as ethylene and higher hydrocarbons is an active area of research as many recent discoveries of natural gas reserves made methane a cheap source of energy with an estimated reserve volume of 215 trillion cubic meters worldwide.[1–3] Due to these new discoveries, methane prices have dropped from \$7–9 USD per million BTU in 2008 to roughly \$2 USD per million BTU in 2020. Readily available amounts of natural gas have risen over 30% in the past 20 years, although transporting it to retail locations remains challenging.[4] Difficulties in transportation of natural gas has resulted in onsite venting and flaring of methane, which results in the release of greenhouse gases CH_4 and CO_2 to the environment apart from methane being wasted.[5,6] Hence, direct conversion of methane to ethylene is highly desired due to ethylene's use as a building block for valuable commodity chemicals, in a wide variety of chemical industries.[7,8] Current technology for producing ethylene primarily centers around naphtha steam-cracking, employing high temperature steam-cracking process as a primary method (>750 °C), which incurs large energy losses and produces significant amounts of CO_2.[3,9,10] Direct catalytic conversion of methane to ethylene allows for skipping of multiple steps that must be completed during steam cracking. For example, direct nonoxidative coupling of methane (NOCM) features methane coupling without requiring an oxygen source into ethylene and aromatic compounds.[11,12] However, NOCM requires high operating temperatures and suffers from ill-defined catalyst mechanisms and significant coke formation.[9] Low temperature oxidative coupling of methane (OCM), pioneered by Keller and Bhasin in 1982, considers methane coupling at temperatures around 750 °C in low O_2 (or other oxidizing agents) gas environments on a catalyst surface.[13] Under OCM conditions, methane coupling to a partial oxidation product such as ethylene is thermodynamically feasible, although further oxidation products like CO and CO_2 are even more favorable. In addition, reaction between the desired product, C_2H_4 and oxygen to produce CO_2 (–1294 kJ mol^{-1} at 800 °C) is far more energetically facile in comparison to methane oxidation to produce CO_2 (–800 kJ mol^{-1} at 800 °C) predicted from HSC calculations (Figure S1, Supporting Information) (collected using HSC Chemistry version 10.0.5.16 software from Outotec). Hence difficulty in achieving ethylene selectivity has remained an issue for OCM.[14–16]

A novel method attempting to circumvent the overoxidation of methane to CO_2 is the electrochemical oxidative coupling of methane (E-OCM).[17–19] The fine-tuning of potential within an electrochemical cell allows for the regulation of oxide ion flux from cathode to anode across the electrolyte material. Further, the extent of oxidation can also be manipulated by the applied bias. Thus E-OCM can theoretically help achieve the partial oxidation of methane to ethylene using oxide-ion conducting electrolytes while restricting the overoxidation to undesirable

L. H. Denoyer, A. Benavidez, F. H. Garzon, K. P. Ramaiyan
Center for Micro-Engineered Materials
Department of Chemical and Biological Engineering
University of New Mexico
Mexico, NM 87106, USA
E-mail: garzon@unm.edu; kramaiyan@unm.edu

The ORCID identification number(s) for the author(s) of this article can be found under https://doi.org/10.1002/admi.202200796.

DOI: 10.1002/admi.202200796

products like CO and CO_2. To this end, we recently demonstrated using an Fe-doped strontium molybdate (SFMO) perovskite catalyst where selective partial oxidation to ethylene is preferred at a specific electrochemical window during E-OCM.[18] Nevertheless, SFMO materials suffered from poor chemical stability under the operating conditions of E-OCM as strontium formed strontium carbonate upon exposure to methane along with significant coke formation. This is a major challenge for many newly developed electrolyte and electrocatalyst systems under high temperature operations as redox stability is essential for durable operation of these devices.[20–27] Fe and Mg codoped $BaMg_{0.33}Nb_{0.67-x}$ $Fe_xO_{3-\delta}$ (BMNF) perovskite material has been demonstrated to resist the carbonate formation under CO_2 environments at elevated temperatures.[28] Further, Fe is incorporated in the crystal lattice and hence should resist coke formation unlike Fe–O based catalyst systems that form carbide and coke in carburizing environments.[29] This is highly relevant for E-OCM, which involves exposure to CH_4, and CO_2 at elevated temperatures.

Hence, we tested this material for chemical stability and E-OCM conversion with three different iron doping levels (x = 0.33, 0.25, and 0.17 (BMNF33, BMNF25, and BMNF17, respectively)). Specifically, we exposed these powders to pure methane at temperatures up to 925 °C and studied their powder X-ray diffraction (PXRD) patterns before and after exposure. Electrochemical measurements were carried out in a home-made button cell set up. For electrochemical measurements, BMNF with varying Fe content in combination with Gd-doped Ceria (GDC) in a 65:35 ratio was used as the anode while $Sr_2Fe_{1.5}Mo_{0.5}O_{6-\delta}$ (SFMO) mixed with GDC in 65:35 ratio was used as the cathode. $La_{0.9}Sr_{0.1}Ga_{0.8}Mg_{0.2}O_{3-\delta}$ (LSGM) pellets with a 0.9 mm thickness and 20 mm diameter were utilized as the electrolyte. E-OCM measurements were carried out at 850 and 925 °C at methane flow rates of 100 SCCM to the anode and O_2 flow rates of 100 SCCM to the cathode. Silver mesh and gold wires were used as current collectors. Electrochemical measurements were also carried out in 4% H_2 balanced in N_2 for comparison purposes.

2. Results and Discussion

2.1. Stability Measurements on $BaMg_{0.33}Nb_{0.67-x}$ $Fe_xO_{3-\delta}$

One of the major challenges for many metal oxide electrodes studied for E-OCM is their chemical stability in carbon-rich environments under high operating temperatures relevant for E-OCM. Hence, investigating the crystallinity of the prepared BMNF materials before and after exposure to methane at elevated temperatures is key in assessing the likelihood of the perovskite to maintain its structure in highly reducing methane environments. The current operating temperatures for the electrochemical oxidative coupling cells may reach as high as 925 °C for testing purposes, with durability tests being done at a maximum of 925 °C for multiple days. However, we want to note here that reducing the operating temperature to as low as 600 °C is increasingly sought after in recent times. We exposed all three prepared BMNF compositions (x = 0.17, 0.25, and 0.33) to methane in a thermogravimetric analysis (TGA) set up and analyzed them through PXRD before and after exposure to CH_4. TGA in air environment is also recorded for comparison purposes. PXRD patterns obtained for as-prepared BMNF powders are shown in **Figure 1**a, which clearly displays the formation of cubic perovskite structure with a space group = *Pm3m* (No. 221) in agreement with previous reports.[28] However, with higher Fe doping as in BMNF33, we observed impurity peaks at 2θ values of 27° and 34°. Hence, we did not prepare compositions with higher Fe doping. The impurity peaks could be attributable to MgO and $Mg_2Fe_2O_5$. Nevertheless, with the incorporation of smaller Fe^{3+} ions over Nb^{5+}, the peak positions shifted towards higher 2θ values as expected from their Shannon ionic radii (Figure S2, Supporting Information).[28] TGA measurements carried out in air in the temperature range of 25 to 900 °C did not show any significant weight change with a maximum weight loss of 0.4% observed for BMFN33 after holding at 900 °C for 1 h (Figure 1c). This could be due to some lattice oxygen lost in equilibrating with its environment. TGA measurements under similar heating conditions in pure CH_4 environment showed similar weight changes with a maximum weight gain of 1.75% observed for BMNF25 while BMNF33 showed a maximum weight loss of 1% at 900 °C (Figure 1d). The marginally higher weight loss under CH_4 environment (1% in CH_4 vs 0.4% in air) could be due to the lattice oxygen on the exposed surface reacting with methane and as a result leaving the crystal structure. The lack of weight gain indicates the possible lack of coke formation during the TGA measurements. SFMO powders under similar operating conditions showed a weight gain of about 40% to 60% that was associated with significant coke formation and crystal structure collapse.[18] To investigate any possible change to crystal structure, we analyzed the CH_4 exposed powders in PXRD. As shown in Figure 1b, the cubic perovskite structure is retained in all three samples and do not show any new peak formation or change in the peak positions associated with the cubic perovskite structure. Interestingly, the impurity peaks observed in the as-prepared BMNF33 also retained their position and relative intensity after exposure to methane in the TGA set up. The ratio between peaks in both as-prepared powders and CH_4 exposed samples remained the same indicating the complete crystallinity retention. Thus, PXRD measurements in combination with TGA provide the first evidence of significant chemical stability for the BMNF material in E-OCM operating conditions. This is in complete contrast to the SFMO powders that formed $SrCO_3$, $SrMO_x$, and MoO_xC_y upon exposure to methane under similar operating conditions.[18] Similar to SFMO, the expected reactions for the constituents of BMNF perovskites such as Ba and Mg upon exposure to methane was the formation of carbonates such as $BaCO_3$, and to some extent $MgCO_3$ as shown in Figure S3 of the Supporting Information along with agglomeration of carbon (coking) on the surface that would result in significant weight gain. This was seen in our work on $Sr_2Fe_{1.5}Mo_{0.5}O_{6-d}$ (SFMO) where up to 60% weight gain was observed in TGA under methane environment along with a complete disintegration of its crystal structure. However, the cubic BMNF perovskite material showed no significant weight change along with complete retention of its crystal structure as observed from Figure 1a–d. The stability of the BMNF structure in methane environment is important due to the constant methane supply to the electrode, and evolution

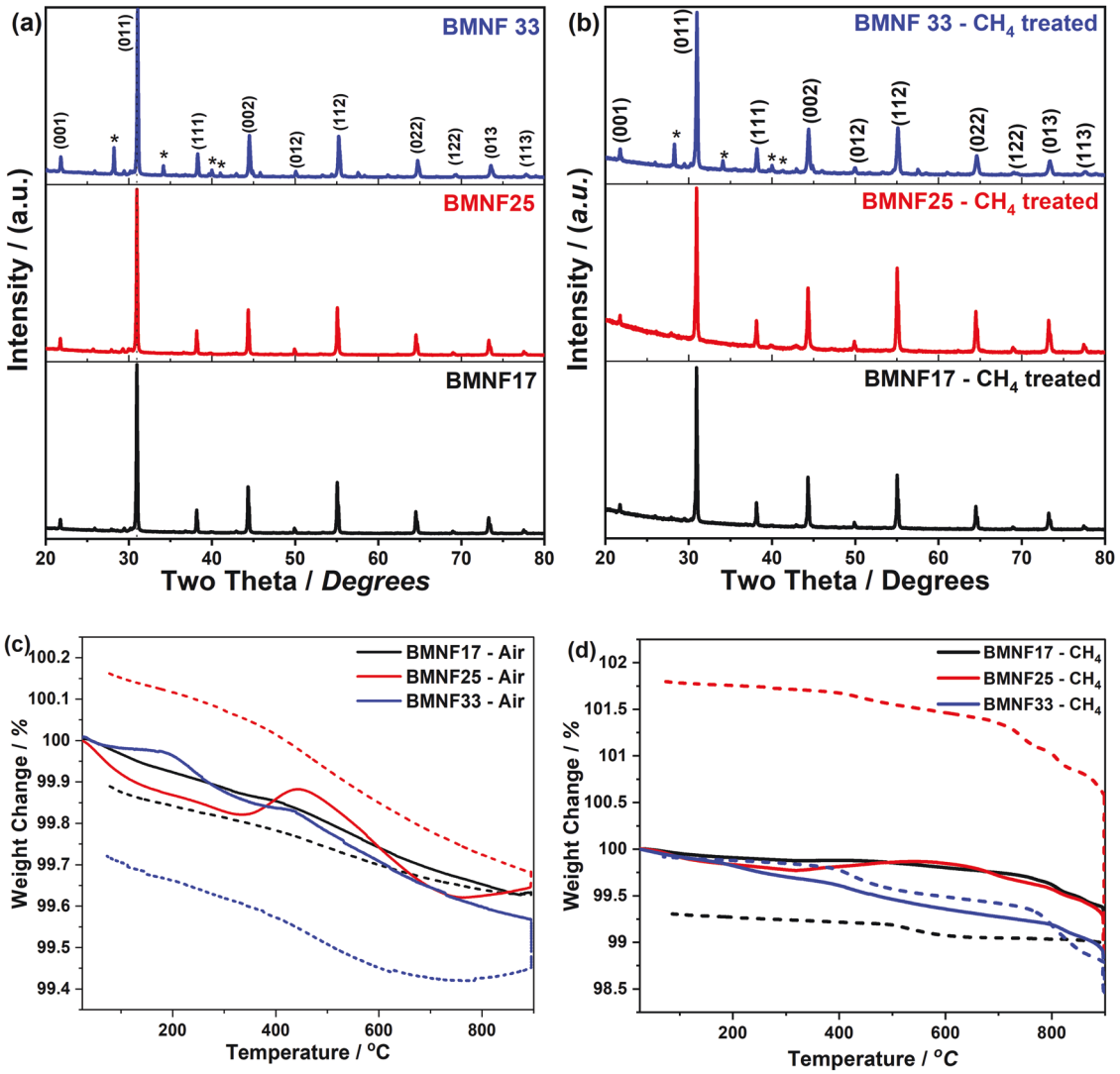

Figure 1. a) PXRD patterns obtained for the as-prepared BMNF materials with various Fe doping and b) PXRD patterns of BMNF materials after exposure to pure methane at 900 °C, c) TGA plots obtained for the as prepared BMNF powders in an air atmosphere, and d) TGA plots obtained for BMNF powders in pure methane atmosphere. The TGA curves in solid indicate the heating direction and curves in dots indicate the cooling response.

of carbon products such as C_2H_4, CO, and CO_2 during OCM and E-OCM processes. High temperature operations render carbonate formations on Mg oxide surface as unfavorable, but unless E-OCM is being used to control the flux of oxide ions within the electrochemical cell, OCM may nevertheless lead to the formation of $BaCO_3$ (Figure S3, Supporting Information). As previously shown, the Gibbs free energy of reaction for CO_2 is $\Delta G_R \approx -800$ kJ mol^{-1} throughout the temperature range being tested (800–900 °C) and would be the dominant product if the reaction is not controlled specifically to produce partial oxidation product such as ethylene by oxide ion flux and applied potentials.[18] To understand this, we carried out temperature programmed reaction measurements where first we exposed the BMNF25 powder to a gas mixture containing 95% CH_4 and 5% O_2 and analyzed the exposed powder for $BaCO_3$ and coke formation while the outlet stream was analyzed by mass spectroscopy (**Figure 2**).

2.2. Temperature Programmed Reaction of CH_4 and O_2 on BMNF

Temperature programmed reaction (TPR) measurements under gas mixtures of CH_4 and O_2 on a catalyst surface will help evaluate the onset temperature of catalytic activity of a new catalyst toward oxidative coupling of methane and provide information about the product distribution. Our TPR measurements were taken by passing a mixture of 95% CH_4:5% O_2 at a flow rate of 100 SCCM and a heating rate of 5 °C min^{-1} to 925 °C followed by a hold at 925 °C for 1 h. We previously reported TPR measurements on SFMO under three different CH_4 to O_2 ratio (100% CH_4, 95% CH_4:5% O_2, and 90% CH_4:10% O_2) which revealed maximum coke formation (100% weight gain) under the 95% CH_4:5% O_2 mixture. SFMO perovskites showed coke formation to start at 800 °C along with other products such as CO, CO_2, H_2, and small quantities of ethylene.[18] Mass spectra analysis on

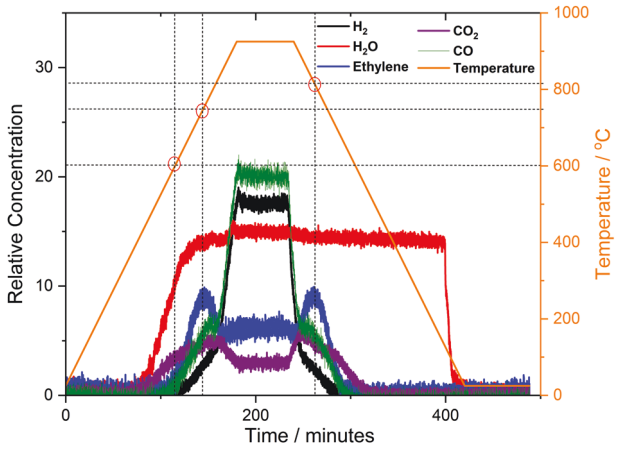

Figure 2. Mass spectroscopic plots obtained for the outlet stream during TPR measurements for the BMNF33 sample in the temperature range of 25–925 °C under 95% CH_4 and 5% O_2.

the outlet stream of TPR measurements obtained with BMNF33 is given in Figure 2, where the onset of ethylene production starts at temperatures as low as 600 °C and reaches the maximum in the temperature range of 750–800 °C. One of the most studied catalyst for OCM reaction, Mn–Na_2WO_4, is reported to show methane conversions at 800 °C at a much higher CH_4 to O_2 ratio.[30,31] Hence, a much lower onset temperature of 600 °C for BMNF33 indicates significant potential for reducing the OCM operating temperatures. Interestingly, the contribution from CO and CO_2 is comparatively smaller than that of ethylene in this temperature range. However, further increase in temperature results in increased CO production. This could be due to a multitude of factors. For example, at ≈900 °C, the dry reformation of methane ($CH_4 + CO_2 = 2CO + H_2$) becomes the thermodynamically preferred reaction that could explain the rise in CO and H_2 concentration while that of ethylene and CO_2 decrease.[32] Further, ethylene is more reactive than methane in general and the decline in ethylene concentration could also be due to possible reaction between produced ethylene and oxygen leading to increased CO production. For comparison, we ran a bare tube measurement with no catalyst in the temperature range of 25–900 °C. As shown in Figure S4 of the Supporting Information, no gas phase reactions take place till the temperature reached ≈875 °C. At 900 °C, the product stream is dominated by H_2O, CO, and H_2 with smaller contributions from ethylene and CO_2. HSC calculation involving 95% CH_4 and 5% O_2 in the investigated temperature range is shown in Figure S5 of the Supporting Information, which indicates the CO to be the major product at temperatures above 600 °C although this process could be kinetically limited. The above provided results clearly indicate the catalytic activity of BMNF perovskites to activate methane toward ethylene production with higher selectivity in the temperature range of 600–800 °C. The carbon atom balance during the TPR measurement is close to 100% reiterating the lack of coke formation with this catalyst. A maximum conversion of 12.5% and a selectivity of 50.3% were observed from BMNF33 catalyst at 800 °C. The weight gain measurements carried out on the sample before and after TPR measurements did not reveal any weight gain further indicating the absence of coking.

2.3. Electrochemical Properties of BMNF Materials

After establishing the chemical stability of BMNF perovskite and its catalytic activity toward methane activation through TGA, PXRD, and TPR measurements, we carried out electrochemical characterization of the BMNF perovskites. The conductivity plots obtained for the three BMNF pellets via electrochemical impedance measurements are given in **Figure 3**a where a maximum conductivity of 17 mS cm^{-1} was obtained for BMNF33 while that observed for BMNF17 is only 7 mS cm^{-1}. The parent $BaMg_{0.33}Nb_{0.67}O_{3-\delta}$ showed a negligible conductivity in the entire investigated temperature range despite aliovalent Mg doping on Nb sites. E-OCM measurements were carried out in a home-made setup with LSGM as electrolyte (0.9 mm thickness and 20 mm diameter), 65:35 mixture of SFMO/GDC as the cathode and a 65:35 mixture of BMNF/GDC as the anode. The electrodes were brush painted on the LSGM pellet, before being sintered at 1175 °C to remove any impurities. LSGM was chosen for electrolyte as the SFMO tends to react with YSZ electrolyte.[33] Cyclic voltammetry (CV) measurements carried out on this cell using BMNF25 as the anode at a scan rate of 1 mV s^{-1} in a wide potential window (–1.5 to 0.9 V against the air reference electrode) is shown in Figure S6 of the Supporting Information while the magnified plot between –1.5 and 0.1 V is given in Figure 3b. The CV plots indicate clear catalytic activity toward methane activation at very low overpotentials near –0.75 V. The full window scan measured between –1.5 and 1.0 V shown in Figure S6 of the Supporting Information indicates a linear rise in current from 0.0 to 1.0 V that suggests a constant surge of oxide ions across the electrolyte that should aid the E-OCM process. The CVs further indicate the durability of BMNF25 under these harsh E-OCM conditions as no significant change in peak intensity or shape is observed over 10 h of electrochemical cycling between –1.5 and 1.0 V. The CV measurements taken after two days of continuous operation remained nearly identical (Figure S7, Supporting Information) further emphasizing the durability of BMNF25. For comparison, SFMO-based electrodes lost all characteristic peaks within few CV cycles.[18] CVs measured in 4% H_2 are given in Figure S8 of the Supporting Information, which indicate none of the characteristic peaks in the –1.3 to –0.5 V region obtained in methane environment. This further demonstrates the role of BMNF25 material in specifically activating methane in a well-defined electrochemical window. These peak position are similar to SFMO-based electrodes, which showed methane activation in the potential range of –0.75 to –0.5 V.[18] The outlet stream of the anode is analyzed continuously by mass spectroscopic measurements to understand the product distribution along with the role of applied bias on E-OCM. The CV results obtained for BMNF25 as a function of time along with the mass spectroscopy results are presented in Figure 3c while that obtained for BMNF25 under 4% H_2 flow is presented in Figure S9 of the Supporting Information. The results clearly indicate the methane activation property of BMNF25 as ethylene and hydrogen are produced under pure CH_4. Interestingly, the methane activation products such as ethylene, CO_2, H_2O, and H_2 all reached their peak value at the maximum positive potential on the studied potential window, i.e., 1.0 V. This is in contrast to our previous results with SFMO-075Fe-based electrodes where, ethylene production

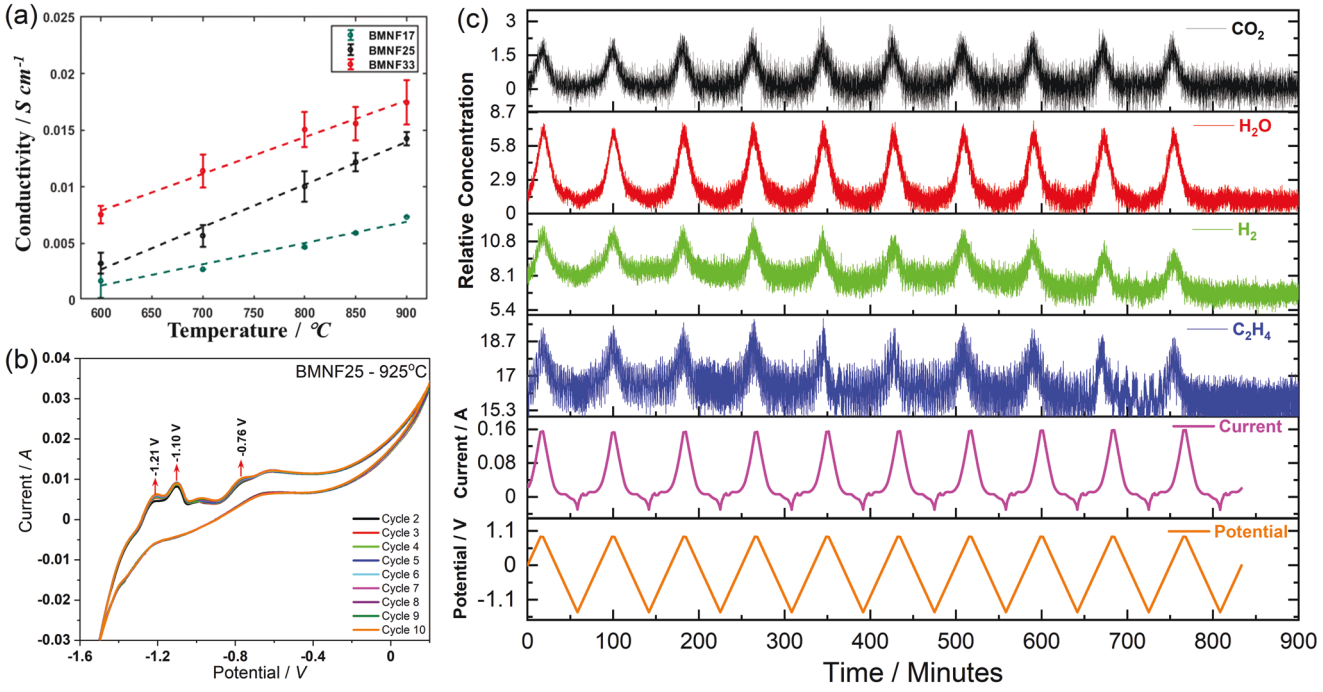

Figure 3. a) Conductivity data obtained for the three BMNF pellets in the temperature range of 600 to 900 °C. b) Cyclic voltammetry curves obtained for BMNF25 under CH_4 cathode environment, and c) current and potential curves along with observed product stream as a function of time for the CV curve presented in Figure S6 of the Supporting Information.

was peaked at –0.75 V in accordance with the methane activation peak in CV. This could possibly be due to the low conductivity of BMNF materials that has resulted in very low current densities at –0.75 V (>10 mA cm^{-2}) in comparison to currents at 1.0 V (≈160 mA cm^{-2}). The low currents could be due to a lower electronic conductivity of BMNF perovskites coupled with low surface area that is normally associated with high-temperature solid state synthesis. For example, the maximum conductivity obtained for BMNF25 through electrochemical impedance measurements is 13 mS cm^{-1} at 900 °C, which is significantly lower than the conductivity of typical solid oxide electrode materials such as LSM, which is about 5.5×10^3 S m^{-1} at 800 °C.[34] Chronoamperometric measurements on this cell once again showed quantifiable ethylene and hydrogen production only at high positive applied potentials (Figure S10, Supporting Information). A maximum ethylene production rate of 277.2 µmol cm^{-2} h^{-1} at a faradaic efficiency (FE) of 20% was observed at 1.0 V for this BMNF25-based cell while the FE for producing CO_2 was 39%. This is about four times higher than the faradaic efficiency obtained with SFMO electrode at this potential, which produced mostly complete oxidation products such as CO_2 and H_2O. This result clearly indicates the propensity of this material to produce ethylene even at high applied biases that tend to favor CO_2 production. We could not satisfactorily calculate the FE toward H_2O production due to water condensing in the lines and its deteriorating effect on the mass spec instrument. While thermocatalytic activity inferred from TPR measurements indicated a methane activation temperature of about 600 °C, E-OCM results are obtained at 925 °C due to the low electrical conductivity of BMNF. Nevertheless, both measurements indicated a better selectivity towards ethylene despite different operating temperatures.

Interestingly, E-OCM measurements with the higher Fe-doped perovskite BMNF33 as the electrode resulted in complete oxidation of methane and the product stream is dominated with CO_2 and H_2O with significantly lower production of ethylene in comparison to both BMNF17 and BMNF25 based electrodes. The higher Fe doping in the BMNF33 could be a reason for this overoxidation of methane towards CO_2. However, the impurities $Mg_2Fe_2O_5$ observed in PXRD with BMNF33 could also have played a role in the overoxidation although it is not clear at this point. CV measurements with BMNF33 in CH_4 indicate less defined peaks while in 4% H_2 show no identifiable peaks (Figure S11a,b, Supporting Information) and mass spectra analysis of the outlet for BMNF33 electrode indicate complete oxidation products such as CO_2 in comparison to BMNF25. Chronoamperometric measurements for BMNF33 once again indicated the complete oxidation products such as CO_2 all indicating the adverse impact of higher Fe doping. Nevertheless, BMNF perovskites showed remarkable chemical stability and maximum E-OCM activity was obtained with BMNF25. Further improvements in electrical conductivity as well as surface area are required for BMNF materials to fully utilize their methane activation properties toward ethylene production. For comparison, we carried out E-OCM measurements with commercial LSM catalyst as anode and CVs obtained under CH_4 and 4% H_2 are given in Figure S12a,b of the Supporting Information. Both CVs are featureless in comparison to BMNF25 electrode under both CH_4 and 4%H_2 environments, once again reaffirming the role of BMNF25 in activating methane.

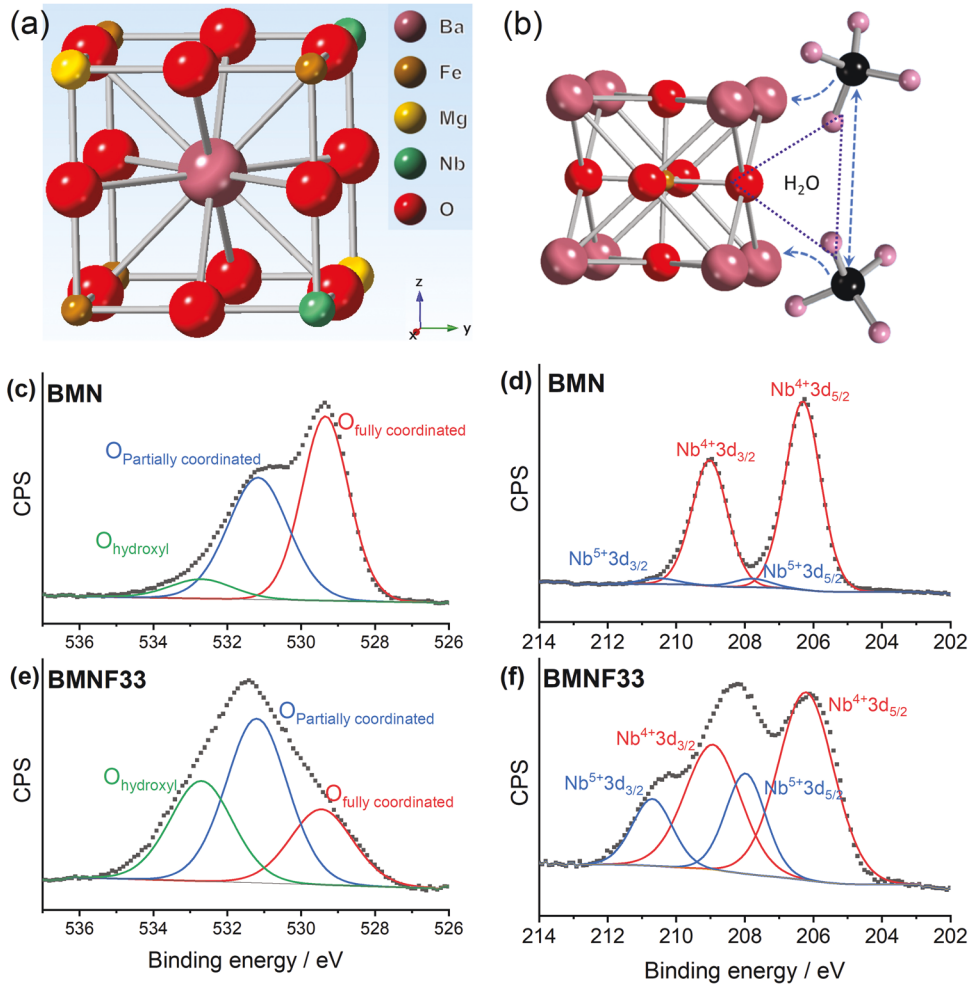

Figure 4. a) CrystalMaker view of the BMNF perovskite, b) schematic representation of methane adsorption on the Ba site in BMNF and water removal using adjacent O atom, XPS data collected for c) O 1s, and d) Nb 3d for the BMN perovskite. e) XPS O1s and f) XPS Nb 3d data collected for BMNF33 perovskite.

2.4. Mechanistic Analysis

The mechanism for catalytic activity toward methane activation is not clear at this point. The cubic perovskite structure created in CrystalMaker is given in **Figure 4**a where both Mg and Fe are incorporated on the Nb site that should result in oxide ion vacancy creation. The doping of Mg^{2+} and Fe^{3+} is expected to occur at the Nb site as their Shannon ionic radii (0.72 and 0.645 Å, respectively) matches better with Nb (Nb^{4+} – 0.68 Å, Nb^{5+} – 0.64 Å) than Ba^{2+} (1.35 Å) which also support oxygen vacancy creation. X-ray photoelectron spectroscopic (XPS) results obtained for BMN and BMNF33 are shown in Figure 4c–f. The incorporation of Mg on Nb sites in BMN has resulted in oxygen vacancy creation as about 50% of the oxygen atoms are partially coordinated that is attributable to neighboring oxygen vacancy. This partially coordinated oxygen concentration increased to 74.9% in BMNF33 indicating a further rise in oxygen vacancy upon Fe doping (Table S1, Supporting Information). Interestingly, in BMN, Nb is mainly in 4+ oxidation state with Nb in 5+ oxidation state contributing only 5%. However, upon Fe doping Nb^{5+} contribution has increased sixfold to ≈30%. Ceramic materials with highly acidic character tend to be stable in carbonate forming environments.[35] For example, the incorporation of acidic Ti^{4+} ions in $SrCo_{0.8}Fe_{0.2}O_{3-\delta}$ is reported to show decreased carbonate formation in pure CO_2 environments at temperatures up to 950 °C.[36] Thus, the highly acidic Nb^{4+} may be the reason for BMN's chemical stability.

Importantly, upon $Fe^{2+/3+}$ incorporation, part of Nb^{4+} is converted to Nb^{5+} that could provide further stability enhancement in carbonate forming environments. On the other hand, among alkaline earth metals, Ba is reported to adsorb methane, CO, and CO_2 in a wide variety of temperatures.[37,38] BMNF has previously been reported for CO_2 sensing application in the temperature range of 500 to 700 °C.[28] Hence, we believe that the barium sites in BMNF would act as adsorption sites for methane while adjacent lattice oxygen help remove two hydrogen atoms as water as shown in the scheme in Figure 4b. This type of surface oxide ions (O^-) reacting with methane is well-known for metal oxide catalysts.[39] However, a continuous removal of surface oxygen and hydrogen from methane will lead to crystal structure collapse, loss of activity, and coke formation. However, we did not observe any change in BMNF crystal structure

and no coke formation was observed either ruling out the continuous removal of oxygen atom from the site. This could occur due to the higher Nb^{5+} concentration that would increase the attraction toward the negative oxide ions and resist their continuous removal. Similarly, Ba-based metal oxides are known to form barium carbonate under carbon rich conditions due to the higher stability of $BaCO_3$ under these conditions.[40,41] Nevertheless, the BMNF perovskite has remained stable under these carbon rich environment and no carbonate or coke formation was observed either. The oxygen mobility in this cubic perovskite is very limited, which may have helped to preserve the crystal structure and the surface oxygen has to be replenished with incoming oxide ions (E-OCM) or oxygen molecule (OCM) for sustained catalytic activity. This is supported by the fact that despite significant oxygen vacancies as evidenced from XPS measurements, BMN shows poor conductivity (>1 μS cm^{-1}). We believe that the low oxide ion mobility and the higher acidity associated with $Nb^{4+/5+}$ ions have helped reduce both coke formation and carbonate formation. The presence of Nb is tend to increase stability under SOFC operating conditions due to its redox stability.[42–44] Scanning electron microscopy (SEM) images obtained for as-prepared and CH_4 exposed samples do not show any morphological change or carbon deposition in EDS measurements (Figure S13, Supporting Information). Another mode of methane activation utilizing oxide ion conducting membranes is the non-Faradaic electrochemical modification of catalytic activity (NEMCA), which is normally associated with Faradaic efficiencies much higher than 100%.[45–47] However, we clearly observed ≈20% Faradaic efficiency for ethylene production indicating the absence of NEMCA mechanism in our E-OCM measurements. Density functional theory based calculations are required for further confirming this proposed mechanism which however is beyond the scope of this study. The high chemical stability along with methane activation properties observed for BMNF perovskites open new opportunities for fine tuning its catalytic activity through various dopants and can also be used as a support for conventional methane activation catalysts where catalyst-support synergy could help achieve better conversion and selectivity toward desired products.

3. Conclusions

We synthesized Mg and Fe codoped barium niobates for application in E-OCM. Our chemical stability studies by TGA, PXRD, and TPR all revealed that all the three prepared compositions possess good chemical stability under conditions relevant for E-OCM. The chemical stability could be due to the increased acidity of $Nb^{4+/5+}$ ions in the crystal lattice. TPR measurements further revealed the onset of ethylene production at ≈600 °C that is significantly lower than well known OCM catalysts. E-OCM measurements were operated at much higher temperatures in order to get good oxide ion conductivity in BMNF. It revealed about four times higher faradaic efficiency towards ethylene production than SFMO electrodes at 1.0 V indicating this materials unique ability to selectively produce ethylene even under extremely oxidizing conditions. XPS measurements indicate a possible valency reorganization for Nb in Fe-doped BMNF compositions that could help improve the chemical stability. Our results demonstrating the methane activation properties of BMNF along with its unique chemical stability under carburizing environments open up new avenues for finding a better catalyst for methane activation under different methodologies.

4. Experimental Section

Materials: BMNF was formed from the following precursors: $BaCO_3$, $C_4Mg_4O_{12}\cdot H_2MgO_2\cdot 5H_2O$ (magnesium carbonate hydroxide pentahydrate), Nb_2O_5, and Fe_2O_3. The electrolyte material LSGM, and $Ce_{0.8}Gd_{0.2}O_2$ (GDC) were purchased from Millipore Sigma. Gold wire used as the leads in the electrochemical cell was purchased from Rio Grande Jewelry Supply. Silver mesh current collectors, high temperature sealing paste (CAP552), thinner for high temperature sealing paste (CAP-552-T), alumina slurry (ALSL), and alumina felt seals were purchased from Fuel Cell Materials. Alumina tubes were purchased from AdValue Technology.

Material Synthesis: The perovskite anode material, $BaMg_{0.33}Nb_{0.67-x}Fe_xO_{3-\delta}$, was produced using solid-state synthesis methods.[28] Initially, the metal oxide and metal carbonate precursors were weighed in stoichiometric ratios to produce 7 g of $BaMg_{0.33}Nb_{0.67-x}Fe_xO_{3-\delta}$ with x values of 0.33, 0.25, 0.17, and 0.00 corresponding to BMNF33, BMNF25, BMNF17, and BMN, respectively. The metal oxide precursors were added to a zirconia ball-milling jar and isopropyl alcohol (IPA) (30 mL) was added (as liquid for ball milling). Each jar contained 16 individual 10 mm diameter zirconia milling balls and powder was milled for 6 h. After milling, ball-milling jars were dried at 120 °C in an oven. The dried powders were calcined at 1000 °C using a 12 h hold and 5 °C min^{-1} heating and cooling rate in a three-phase furnace. The calcined powders were further ball milled for 6 h in IPA followed by drying at 120 °C. Thus, obtained powders were pressed into two individual pellets using a 12 mm die. Both uniaxial pressing, followed by isostatic pressing were used. The initial uniaxial pressing was done at 1000 psi for 3 min followed by isostatic pressing done at 240 MPa for 3 min. Each pressed pellet weighed ≈2.0 g. The pellets were soaked in excess parent powder in an alumina crucible for calcining. The pellets were calcined at 1400 °C for 24 h with a 5 °C min^{-1} heating and cooling rate in a Carbolite tube furnace. After this process, the pellets were used for further measurements. BMNF powder is typically black in color, with lighter shades corresponding to a lower iron concentration. The Fe free BMN is yellowish in color. The cathode $Sr_2Fe_{1.5}Mo_{0.5}O_{6-\delta}$ (SFMO) powders were prepared by a microwave-assisted combustion methods as described in the previous work.[19] SFMO was chosen due to its very high electrical conductivity and compatibility with LSGM.[33] The LSGM pellets for electrolyte application were prepared from commercially obtained LSGM powder. About 1.6 g of LSGM powder was pressed uniaxially using a 25 mm die. The pressed powder was then pressed in the isostatic press at 240 MPa for 3 min followed by sintering at 1175 °C for 12 h using a 3 °C min^{-1} heating and cooling rate.

Physical Characterization: BMNF powders were characterized by PXRD, TGA, SEM, and XPS measurements. TGA measurements were carried out using TA Q600 SDT instrument in air and in pure methane environments with flow rate of 50 mL min^{-1} in the temperature window of 25 to 900 °C at a heating and cooling rate of 5 °C min^{-1} and held at 900 °C for 1 h. XPS measurements were performed on a Kratos Ultra DLD spectrometer using a monochromatic Al Kα source operating at 150 W (1486.6 eV). The operating pressure was 5×10^{-9} Torr. Survey spectra were acquired at a pass energy of 160 eV and high-resolution spectra were acquired at a pass energy of 20 eV. XPS data were processed using Casa XPS software. X-ray diffraction measurements were done in a PANalytical Xpert Pro instrument using Cu Kα radiation and operating at 40 kV and 40 mA on a zero-background holder. SEM-EDX measurements carried out on Hitachi S-5200 scanning electron microscope.

Electrochemical Measurements: BMNF (200 mg) was mixed with $Ce_{0.8}Gd_{0.2}O_2$ (GDC) (100 mg), terpineol (630 mg), and cellulose (70 mg) to produce 1 g of BMNF ink. This mixture was probe sonicated using a Tekmar probe sonicator for 6 min in 30 s intervals (on/off). The SFMO cathode was made using SFMO (200 mg) and GDC (100 mg) with terpineol (630 mg) as a dispersant and cellulose (70 mg) added for induced porosity. The resultant mixture was ultrasonically mixed before electrode painting. The BMNF anode was brush-coated onto the LSGM electrolyte in a 1×1 cm^2 electrode area. Three layers of material were coated onto the electrolyte, with a heat gun used to dry each subsequent layer. The SFMO cathode was brush-coated with the same specifications. This cell was placed into a 3-phase furnace and heat-treated at 1175 °C for 12 h in air at a 3 °C min^{-1} heating rate. After heat treatment, silver mesh current collectors were applied to both the anode and cathode of this cell. Each silver mesh current collector was interwoven with the gold leads and is attached to the respective electrode using silver paste. After the silver paste dries (for at least 20 min), the cell was placed on the alumina tube setup using the high-temperature sealing paste mixed with thinner, along with an alumina felt seal to make a leak-free attachment of the cell to the alumina tubing. The cell was left in the open-air environment for 4 or more hours (to allow for the paste to dry) and placed in the cell-testing furnace. Here, the cell undergoes in situ heat treatment at 95 and 260 °C for 2 h each, followed by sintering at 550 °C for 1 h. The cell was then heated to 800 °C after which a 100 SCCM of 4% H_2 balanced in N_2 was introduced anode-side and 100 SCCM of UHP O_2 was introduced to the cathode side. After 1 h under 4% H_2, 100 SCCM UHP CH_4 was introduced to the anode side for electrochemical oxidative coupling of methane experiments. The outlet of the EC-OCM set up was continuously fed into a Cirrus mass spectrometer for regular monitoring and periodically analyzed by an SRI 8610C Gas chromatography instrument. A schematic representation of the electrochemical setup is given in Figure S14 of the Supporting Information. Electrochemical experiments were carried out using a Gamry reference 600 instrument.

Statistical Analysis: Conductivity values from impedance measurements were represented as the average values with upper and lower limit data given in the error bar.

Supporting Information

Supporting Information is available from the Wiley Online Library or from the author.

Acknowledgements

The authors thank the NSF – Center for Innovative and Strategic Transformation of Light Alkane Resources (CISTAR) (NSF – CISTAR Award No. EEC-1647722) for funding this work.

Conflict of Interest

The authors declare no conflict of interest.

Author Contributions

L.D. and K.P.R. carried out synthesis and electrochemical experiments, A.B. carried out XPS measurements, K.P.R. wrote the manuscript, and F.G. edited the manuscript and supervised the work.

Data Availability Statement

The data that support the findings of this study are available from the corresponding author upon reasonable request.

Keywords

barium niobate, electrocatalyst, methane, oxidative coupling, perovskite

Received: April 14, 2022
Revised: July 22, 2022
Published online: August 26, 2022

[1] J. H. Lunsford, *Catal. Today* **2000**, *63*, 165.
[2] W. Pang, Y. Wang, Z. Jin, *Energy Fuels* **2021**, *35*, 8456.
[3] Z. Liang, T. Li, M. Kim, A. Asthagiri, J. F. Weaver, *Science* **2017**, *356*, 299.
[4] Y. Gensterblum, A. Ghanizadeh, R. J. Cuss, A. Amann-Hildenbrand, B. M. Krooss, C. R. Clarkson, J. F. Harrington, M. D. Zoback, *J. Unconv. Oil Gas Resour.* **2015**, *12*, 87.
[5] J. A. Arminio-Ravelo, M. Escudero-Escribano, *Curr. Opin. Green Sustainable Chem.* **2021**, *30*, 100489.
[6] T. Lauvaux, C. Giron, M. Mazzolini, A. D'aspremont, R. Duren, D. Cusworth, D. Shindell, P. Ciais, *Science* **2022**, *375*, 557.
[7] Y. Gao, L. Neal, D. Ding, W. Wu, C. Baroi, A. M. Gaffney, F. Li, *ACS Catal.* **2019**, *9*, 8592.
[8] S. Yuan, Y. Li, J. Peng, Y. M. Questell-Santiago, K. Akkiraju, L. Giordano, D. J. Zheng, S. Bagi, Y. Román-Leshkov, Y. Shao-Horn, *Adv. Energy Mater.* **2020**, *10*, 2002154.
[9] N. Levin, J. Lengyel, J. F. Eckhard, M. Tschurl, U. Heiz, *J. Am. Chem. Soc.* **2020**, *142*, 5862.
[10] D. Richard, Y.-C. Huang, C. G. Morales-Guio, *Curr. Opin. Electrochem.* **2021**, *30*, 100793.
[11] N. Kosinov, E. J. M. Hensen, *Adv. Mater.* **2020**, *32*, 2002565.
[12] Y. Nishikawa, H. Ogihara, I. Yamanaka, *ChemistrySelect* **2017**, *2*, 4572.
[13] G. E. Keller, M. M. Bhasin, *J. Catal.* **1982**, *73*, 9.
[14] P. Schwach, M. G. Willinger, A. Trunschke, R. Schlögl, *Angew. Chem., Int. Ed.* **2013**, *52*, 11381.
[15] L. Mleczko, U. Pannek, V. M. Niemi, J. Hiltunen, *Ind. Eng. Chem. Res.* **1996**, *35*, 54.
[16] A. M. Arinaga, M. C. Ziegelski, T. J. Marks, *Angew. Chem., Int. Ed.* **2021**, *60*, 10502.
[17] G. Li, Y. Fang, C. Arges, C. Plaisance, J. Flake, *J. Electrochem. Soc.* **2020**, *167*, 155503.
[18] K. P. Ramaiyan, L. H. Denoyer, A. Benavidez, F. H. Garzon, *Commun. Chem.* **2021**, *4*, 139.
[19] C. Zhu, S. Hou, X. Hu, J. Lu, F. Chen, K. Xie, *Nat. Commun.* **2019**, *10*, 1173.
[20] A. Hauch, S. D. Ebbesen, S. H. Jensen, M. Mogensen, *J. Mater. Chem.* **2008**, *18*, 2331.
[21] G. Iqbal, H. Guo, B. S. Kang, O. A. Marina, *Int. J. Appl. Ceram. Technol.* **2011**, *8*, 13.
[22] L. Ma, Y. Wang, W. Li, B. Guan, H. Qi, H. Tian, L. Zhou, H. A. De Santiago, X. Liu, *J. Power Sources* **2021**, *488*, 229458.
[23] Y. Wang, W. Li, L. Ma, W. Li, X. Liu, *J. Mater. Sci. Technol.* **2020**, *55*, 35.
[24] K. N. Grew, Y. S. Chu, J. Yi, A. A. Peracchio, J. R. Izzo, Y. Hwu, F. De Carlo, W. K. S. Chiu, *J. Electrochem. Soc.* **2010**, *157*, B783.
[25] G. J. Nelson, K. N. Grew, J. R. Izzo, J. J. Lombardo, W. M. Harris, A. Faes, A. Hessler-Wyser, J. Van herle, S. Wang, Y. S. Chu, A. V. Virkar, W. K. S. Chiu, *Acta Mater.* **2012**, *60*, 3491.
[26] M. Z. Khan, R.-H. Song, A. Hussain, S.-B. Lee, T.-H. Lim, J.-E. Hong, *J. Eur. Ceram. Soc.* **2020**, *40*, 1407.
[27] B. J. M. Sarruf, J.-E. Hong, R. Steinberger-Wilckens, P. E. V. de Miranda, *Int. J. Hydrogen Energy* **2020**, *45*, 5297.
[28] R. Kannan, S. Mulmi, V. Thangadurai, *J. Mater. Chem. A* **2013**, *1*, 6874.

[29] F. Bonnet, F. Ropital, P. Lecour, D. Espinat, Y. Huiban, L. Gengembre, Y. Berthier, P. Marcus, *Surf. Interface Anal.* **2002**, *34*, 418.
[30] J. Liu, J. Yue, M. Lv, F. Wang, Y. Cui, Z. Zhang, G. Xu, *Carbon Resour. Convers.* **2022**, *5*, 1.
[31] S. Da Ros, T. Barbalho Fontoura, M. Schwaab, N. J. Castro de Jesus, J. C. Pinto, *Process* **2021**, *9*, 2196.
[32] I. V. Yentekakis, P. Panagiotopoulou, G. Artemakis, *Appl. Catal., B* **2021**, *296*, 120210.
[33] Q. Liu, X. Dong, G. Xiao, F. Zhao, F. Chen, *Adv. Mater.* **2010**, *22*, 5478.
[34] O. O. Agbede, K. Hellgardt, G. H. Kelsall, *Mater. Today Chem.* **2020**, *16*, 100252.
[35] Z. Tao, Z. Zhu, H. Wang, W. Liu, *J. Power Sources* **2010**, *195*, 3481.
[36] Q. Zeng, Y. Zuo, C. Fan, C. Chen, *J. Membr. Sci.* **2009**, *335*, 140.
[37] G. Sethia, R. S. Somani, H. C. Bajaj, *RSC Adv.* **2015**, *5*, 12773.
[38] E. Akbari, S. M. Alavi, M. Rezaei, A. Larimi, *Int. J. Hydrogen Energy* **2021**, *46*, 5181.
[39] J. A. Roos, S. J. Korf, R. H. J. Veehof, J. G. van Ommen, J. R. H. Ross, *Appl. Catal.* **1989**, *52*, 131.
[40] D. Dissanayake, J. H. Lunsford, M. P. Rosynek, *J. Catal.* **1993**, *143*, 286.
[41] R. Kannan, K. Singh, S. Gill, T. Fürstenhaupt, V. Thangadurai, *Sci. Rep.* **2013**, *3*, 2138.
[42] W. Zhang, Y. Zhou, E. Liu, Y. Ding, Z. Luo, T. Li, N. Kane, B. Zhao, Y. Niu, Y. Liu, M. Liu, *Appl. Catal., B* **2021**, *299*, 120631.
[43] J. Wang, L. Jiang, X. Xiong, C. Zhang, X. Jin, L. Lei, K. Huang, *J. Electrochem. Soc.* **2016**, *163*, F891.
[44] S. Wang, Y. Chen, S. Fang, L. Zhang, M. Tang, K. An, K. S. Brinkman, F. Chen, *Chem. Mater.* **2014**, *26*, 2021.
[45] M. Stoukides, *Res. Chem. Intermed.* **2006**, *32*, 187.
[46] K. Otsuka, S. Yokoyama, A. Morikawa, *Chem. Lett.* **1985**, *14*, 319.
[47] V. O. Igenegbai, R. Almallahi, R. J. Meyer, S. Linic, *ACS Energy Lett.* **2019**, *4*, 1465.